

Extracting information from ocean color

B. B. Cael¹, Kelsey Bisson², Emmanuel Boss³, and Zachary K. Erickson⁴

¹National Oceanography Centre, Southampton, UK

²Oregon State University, Corvallis, OR, USA

³University of Maine, Orono, ME, USA

⁴NOAA Pacific Marine Environmental Laboratory, Seattle, WA, USA

Key Points:

- In situ hyperspectral $R_{rs}(400-700\text{nm})$ have 4 degrees of freedom & are predicted within uncertainties by MODIS & SeaWiFS wavebands.
- Degrees of freedom are lost upscaling to global satellite climatologies and again to $R_{rs}(\lambda)$ -derived products like chlorophyll.
- Information exists in satellite $R_{rs}(\lambda)$ that's underutilized by products' algorithms. Future algorithms must consider correlations carefully.

This is a non-peer reviewed preprint submitted to EarthArXiv.

Corresponding author: B. B. Cael, cael@noc.ac.uk

Abstract

Products derived from remote sensing reflectances ($R_{rs}(\lambda)$), e.g. chlorophyll, phytoplankton carbon, euphotic depth, or particle size, are widely used in oceanography. Problematically, $R_{rs}(\lambda)$ may have fewer degrees of freedom (DoF) than measured wavebands or derived products. A global sea surface hyperspectral $R_{rs}(\lambda)$ dataset has DoF=4. MODIS-like multispectral equivalent data also have DoF=4, while their SeaWiFS equivalent has DoF=3. Both multispectral-equivalent datasets predict individual hyperspectral wavelengths' $R_{rs}(\lambda)$ within nominal uncertainties. Remotely sensed climatological multispectral $R_{rs}(\lambda)$ have DoF=2, as information is lost by atmospheric correction, shifting to larger spatiotemporal scales, and/or more open-ocean measurements, but suites of $R_{rs}(\lambda)$ -derived products have DoF=1. These results suggest that remote sensing products based on existing satellites' $R_{rs}(\lambda)$ are not independent and should not be treated as such, that existing $R_{rs}(\lambda)$ measurements hold unutilized information, and that future multi- or especially hyper-spectral algorithms must rigorously consider correlations between $R_{rs}(\lambda)$ wavebands.

Plain Language Summary

The reflectance of sunlight from the ocean can be observed from satellites and is used to derive many biologically-relevant parameters, such as the concentration of chlorophyll in the upper ocean. Reflectances are currently observed at about ten different wavelengths, but this will soon be expanded to hundreds with the upcoming launch of a new ocean color satellite, PACE, in early 2024. Many new algorithms are being proposed to make use of the wealth of ocean color data which will be provided. However, there are strong correlations between reflectances at different wavelengths; these correlations mean there will be far fewer products that can be independently derived than there will be reflectance wavelengths observed. Here we use a ship-based measurements similar to what will be provided from PACE to suggest that, on a global scale, only a few independent variables can be calculated from hundreds of reflectance wavelengths. Current and past satellites provide a similar amount of independent data to what is projected from PACE. We then show that, on a global scale, a set of six derived parameters only contains one independent piece of information, suggesting that more information exists in ocean color data than is being currently used.

1 Introduction

Ocean color satellites have revolutionized the study of ocean ecology and biogeochemistry in recent decades by providing a near-continuous global picture of surface ocean properties (Hovis et al., 1980; O'Reilly et al., 1998). Satellites measure the spectral radiance emanating from the ocean and atmosphere. Remote sensing reflectance ($R_{rs}(\lambda)$) is obtained following the removal of the contribution of atmospheric and surface effects and normalization to downwelling solar irradiance. Algorithms have been developed to estimate numerous biogeochemically-relevant surface variables from $R_{rs}(\lambda)$, such as chlorophyll concentration (Chl, [$\mu\text{g/L}$]) (O'Reilly et al., 1998; Hu et al., 2012), the spectral slope of the particle size distribution (ξ) (Kostadinov et al., 2009), the concentrations of phytoplankton and particulate organic and inorganic carbon (C_{phyto} , POC, and PIC, [$\mu\text{g/L}$]) (Graff et al., 2015; Evers-King et al., 2017; Mitchell et al., 2017), euphotic layer depth (Z_{eu} [m]) (Lee et al., 2007), and, using additional input variables, net primary production (NPP, [$\text{mg/m}^2\text{d}$]) (Behrenfeld & Falkowski, 1997; Silsbe et al., 2016; Westberry et al., 2008). Such products are used in a wide variety of applications, such as validation of complex ocean ecosystem and biogeochemistry models (Dutkiewicz et al., 2020; Cael et al., 2021) or as inputs for simpler models that predict other variables such as vertical particulate organic carbon fluxes from ocean color (Siegel et al., 2014; Cael et al., 2017; DeVries & Weber, 2017; Nowicki et al., 2022; Bisson et al., 2020).

Existing $R_{rs}(\lambda)$ data are multispectral, meaning they are measured within several individually determined wavebands. Derived products generally rely only on a subset of these wavebands and are commonly expressed as functions of band ratios between just two wavelengths (e.g. Hu et al., 2012). Some algorithms attempt to simultaneously estimate multiple products to match the full spectrum of $R_{rs}(\lambda)$; for example, the Generalized Inherent Optical Properties (GIOP) approach (Werdell et al., 2013) uses known and assumed spectral shapes of backscattering and absorption from different optical constituents to estimate the suite of products that best represents the observed $R_{rs}(\lambda)$. However, the most widely used products, such as for Chl and POC, treat all outputs as independent quantities and are fully empirical.

Correlations between $R_{rs}(\lambda)$ at different wavebands can be quite strong (Huot & Antoine, 2016), depending also on the spatiotemporal scales considered (see §3). This presents multiple potential issues for both users and developers of ocean color derived products. If multiple products are used simultaneously and treated as independent when they are in fact not, this can lead to overconfidence in model skill or miscalculation of uncertainties. An unintended consequence of treating satellite products independently within models is a functional limit on model complexity. Adding different (yet correlated) satellite products to a model can result in model output redundancy (Bisson et al., 2020). These issues will only be exacerbated by the hyperspectral resolution of the next generation of ocean color satellites, namely the Plankton, Clouds, Aerosols and Ecosystems (PACE) satellite scheduled to launch January 2024 (Werdell et al., 2019). In addition to the common suite of multispectral products, PACE also plans to move beyond chlorophyll and enable characterizations of phytoplankton communities (e.g. Chase et al., 2017), substantially increasing the number of products available from $R_{rs}(\lambda)$.

The strong correlations among $R_{rs}(\lambda)$ wavelengths can be framed in terms of the degrees of freedom (DoF) of $R_{rs}(\lambda)$ measurements and suites of derived products. DoF represents the effective number of dimensions of a dataset after accounting for correlations and uncertainties between variables and is in essence the number of independent variables in that dataset. It has been shown that the DoF of globally distributed near-surface measured hyperspectral absorption spectra is about five (Cael et al., 2020). This could be considered a possible upper limit for the DoF of satellite-measured $R_{rs}(\lambda)$ given higher uncertainties on satellite measurements – particularly associated with atmospheric correction (Bisson et al., 2021; Cael et al., 2020). The DoF of PACE’s hyperspectral measurements might then be expected to be much lower than the number of wavelengths for which it will measure $R_{rs}(\lambda)$, which will appreciably affect how hyperspectral satellite $R_{rs}(\lambda)$ products should be constructed. For both existing and future satellite $R_{rs}(\lambda)$, in other words, understanding the DoF of $R_{rs}(\lambda)$ measurements and derived products is crucial for appropriate usage and optimal construction of such products.

Here we investigate the DoF of $R_{rs}(\lambda)$. We first find that a global sea surface hyperspectral $R_{rs}(\lambda)$ database has four DoF. Coarsening hyperspectral $R_{rs}(\lambda)$ to their MODIS (Moderate Resolution Imaging Spectrometer) equivalent retains four DoF, though the SeaWiFS (Sea-viewing Wide Field of view Sensor) equivalent only has three DoF. Both of these multispectral equivalents can, however, predict individual hyperspectral $R_{rs}(\lambda)$ wavelengths within nominal uncertainties for satellite sensors. We then consider climatological $R_{rs}(\lambda)$ and derived products. We find that both MODIS-Aqua and SeaWiFS $R_{rs}(\lambda)$ have two DoF at the climatological scale, suggesting that $R_{rs}(\lambda)$ complexity is lost either through atmospheric correction, relatively more inclusion of open-ocean data, or averaging over larger scales in space and time. Suites of derived products, however, only retain one DoF. This latter result suggests that derived products should not be treated as independent by users. We close by discussing the substantial implications these findings have for the construction and use of ocean color products, from both existing and future $R_{rs}(\lambda)$.

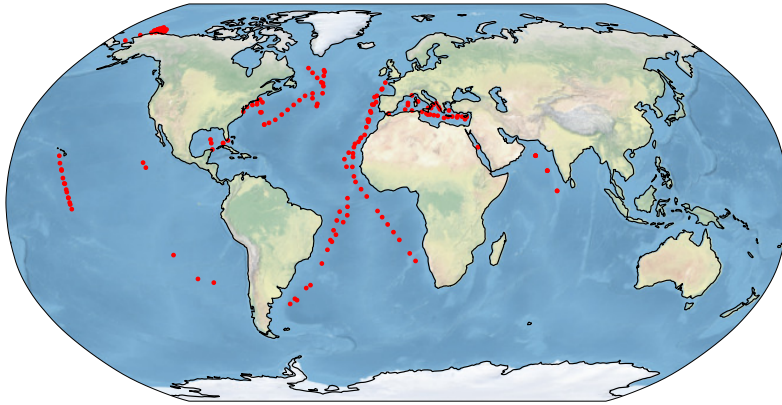


Figure 1. Locations of the 191 stations considered in this study (red dots).

117 2 Sea surface R_{rs} : hyperspectral versus multispectral

118 We first analyze a global sea surface hyperspectral $R_{rs}(\lambda)$ dataset to determine its
 119 DoF and how the DoF depends on spectral resolution (Chase et al., 2017; Kramer et al.,
 120 2022). The dataset includes $R_{rs}(\lambda)$ data at 191 locations at an effective 3.35 nm reso-
 121 lution (Chase et al., 2017) from 400–800 nm, linearly interpolated to 1 nm (Figure 1).
 122 We trimmed spectra to 700nm due to the large fraction of missing values $>700\text{nm}$; note
 123 that most of the non-empty values $>700\text{nm}$ are zeros and the non-zero-non-empty val-
 124 ues, with a median of $<4 \times 10^{-5} \text{ sr}^{-1}$, have very small signal-to-noise ratios. The dataset
 125 includes measurements taken from 2004 to 2018 evenly distributed across months of the
 126 year, and from all major ocean basins ranging in latitude from 41°S to 74°N . We also
 127 compare these data to their MODIS-Aqua and SeaWiFS multispectral equivalents by
 128 convoluting the hyperspectral $R_{rs}(\lambda)$ with the MODIS-Aqua and SeaWiFS spectral re-
 129 sponse functions (available at [https://oceancolor.gsfc.nasa.gov/docs/rsr/HMODISA](https://oceancolor.gsfc.nasa.gov/docs/rsr/HMODISA_RSRs.txt)
 130 [_RSRs.txt](https://oceancolor.gsfc.nasa.gov/docs/rsr/SeaWiFS_RSRs.txt) and https://oceancolor.gsfc.nasa.gov/docs/rsr/SeaWiFS_RSRs.txt)
 131 to generate 10-waveband and 6-waveband datasets which correspond to what each in-
 132 strument would have measured from the same optical input that the radiometer received
 133 when generating the hyperspectral $R_{rs}(\lambda)$ data.

134 We then apply principal component analysis (PCA) (Wold et al., 1987) to these
 135 301-, 10- and 6-dimensional $R_{rs}(\lambda)$ datasets. PCA is a widely used method to reduce
 136 the dimensionality of datasets by identifying orthogonal vectors that explain the most
 137 variance in the data. PCA is linear in nature, which may result in an overestimation of
 138 effective dimensions by poorly approximating non-linear relationships between variables
 139 (e.g. a PCA performed on the pair (x, y) where $y = x^2$ will yield two DoF). Nonlin-
 140 ear generalizations do exist (Weinberger et al., 2004; Scholz et al., 2008), though these
 141 are less widely applied due to their additional complexity and computational require-
 142 ments that make interpretation challenging. One may therefore consider the DoF we re-
 143 port to be upper bounds. We perform a PCA on each $R_{rs}(\lambda)$ dataset, standardizing each
 144 first by subtracting from each waveband its mean and then dividing by its standard de-
 145 viation. This results in a percentage of total variance explained by each component. We
 146 use the broken-stick rule to choose the DoF, which states that the DoF is equal to the
 147 number of components that explain more variance than would be expected by randomly
 148 distributed data; this method was shown to be more consistent than a suite of others in
 149 a comparison (Jackson, 1993). These results can be shown visually as a ‘scree’ plot, which
 150 plots the percentage of variance explained by each component and for randomly distributed
 151 data; the DoF is the number of components with a higher percentage of variance explained
 152 than would be expected for randomly distributed data. Our figures also visibly demon-

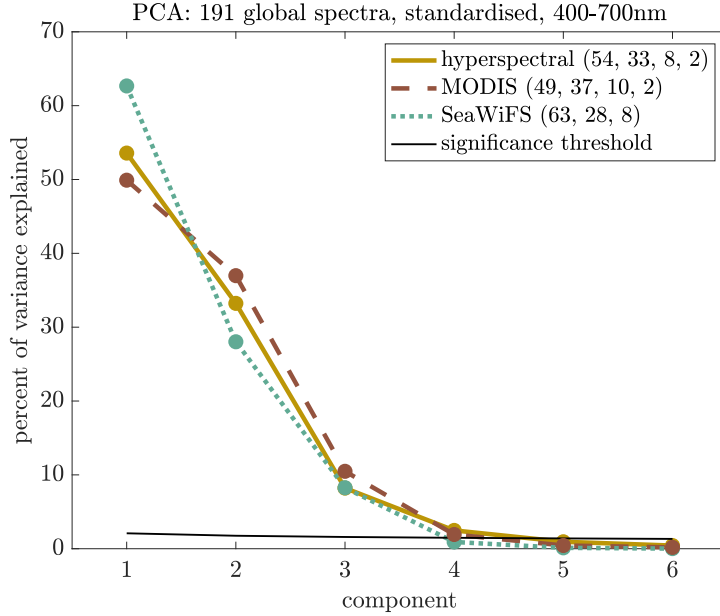


Figure 2. Scree plot of percent variance explained versus component for hyperspectral $R_{rs}(\lambda)$ dataset and MODIS-Aqua and SeaWiFS equivalents calculated from their spectral response functions. Black line indicates broken-stick significance threshold for hyperspectral data; numbers in legend give percent variance explained for each mode above this threshold in each case.

153 strate that one would get the same results from using the scree plot rule, which states
 154 that the DoF is equal to the number of components not sitting on the straight line made
 155 by the higher-order components, and was found to consistently capture the correct DoF
 156 plus one when the first point on this straight line was included (Jackson, 1993).

157 PCA analysis reveals that the hyperspectral in situ $R_{rs}(\lambda)$ dataset has four DoF
 158 (Figure 2); the first four components explain 54%, 33%, 8%, and 2%, totalling 97%, of
 159 the variance. The first four MODIS-Aqua equivalent $R_{rs}(\lambda)$ principal components have
 160 very similar percentages of variance explained: 49%, 37%, 10%, and 2%, totalling 99%
 161 of the total variance. In contrast, the first three SeaWiFS equivalent $R_{rs}(\lambda)$ principal
 162 components explain 63%, 28%, and 8%, totalling 99%, of the variance. This suggests
 163 that the hyperspectral $R_{rs}(\lambda)$ have four DoF, or four independent variables within the
 164 data, and that these four variables are effectively captured when reducing spectral res-
 165 olution to the ten MODIS-Aqua wavebands, but not to the six SeaWiFS wavebands.

166 The ability of coarsened, MODIS-equivalent data to obtain the same number of DoF
 167 as the hyperspectral dataset is further supported by predictions of hyperspectral $R_{rs}(\lambda)$
 168 from multispectral equivalents. To illustrate this, for each hyperspectral wavelength we
 169 perform a multivariate linear regression of $R_{rs}(\lambda)$ at that wavelength regressed against
 170 $R_{rs}(\lambda)$ at each waveband of both the MODIS-Aqua and SeaWiFS equivalent $R_{rs}(\lambda)$. We
 171 then calculate the root-mean-square-error (RMSE) of these regressions. For all wavelengths
 172 below 578 nm in the SeaWiFS case and 582 nm in the MODIS-Aqua case, the RMSE
 173 is smaller – and for many, much smaller – than 5% of the mean $R_{rs}(\lambda)$ at that wavelength,
 174 where 5% is a nominal relative uncertainty for satellite $R_{rs}(\lambda)$ (Figure 3). Even for wave-
 175 lengths greater than this, the RMSE is still very small in absolute terms, $<0.00007 \text{ sr}^{-1}$,
 176 far smaller than the nominal 0.0003 sr^{-1} absolute error for 1km-by-1km pixels for PACE
 177 (Gordon & Wang, 1994). These small errors in predicting hyperspectral $R_{rs}(\lambda)$ from its
 178 multispectral equivalent underscore the extent to which different wavelengths’ $R_{rs}(\lambda)$

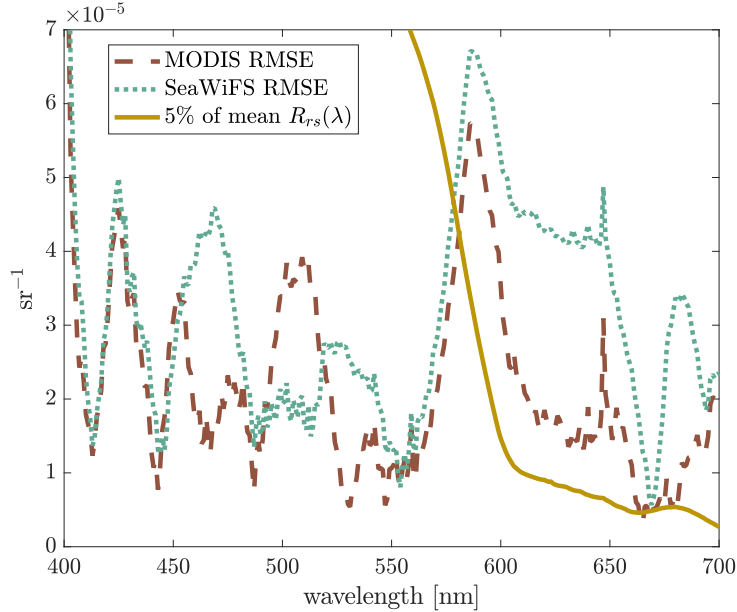


Figure 3. Root-mean-square-error of multivariate linear regressions of each hyperspectral wavelength versus the MODIS-Aqua and SeaWiFS equivalent $R_{rs}(\lambda)$. Solid line is 5% of the mean of each wavelength’s hyperspectral $R_{rs}(\lambda)$.

179 are correlated and demonstrate the ability of MODIS-Aqua equivalent multispectral $R_{rs}(\lambda)$
 180 to preserve the dimensionality of hyperspectral $R_{rs}(\lambda)$. The fact that SeaWiFS-like $R_{rs}(\lambda)$
 181 can accurately predict hyperspectral $R_{rs}(\lambda)$ to within PACE uncertainties but has fewer
 182 DoF than the in situ hyperspectral dataset is a reflection of the lower uncertainty on the
 183 in situ dataset than the expected PACE $R_{rs}(\lambda)$, and suggests that PACE $R_{rs}(\lambda)$ may
 184 have fewer DoF than the in situ hyperspectral dataset.

185 We also note that excluding wavelengths 651–700nm affects the DoF numbers presented here but not our conclusions. A choice of an upper limit of 650nm would be based
 186 on the fact that for all wavelengths above 648nm, >95% of measurements are below 0.0003
 187 sr^{-1} , the nominal uncertainty of a 1km-by-1km pixel for PACE (Gordon & Wang, 1994).
 188 Repeating this analysis over 400–650nm results in hyperspectral and MODIS-Aqua-equivalent
 189 $R_{rs}(\lambda)$ data having three DoF, and SeaWiFS-equivalent $R_{rs}(\lambda)$ data having two DoF.
 190 This suggests that there is one DoF in the 651–700nm range that is picked up by hyper-
 191 spectral and multispectral $R_{rs}(\lambda)$ alike; however, the $R_{rs}(\lambda)$ values are small enough (mean
 192 and median both $<1.2 \times 10^{-4} \text{ sr}^{-1}$ for all wavelengths 651–700nm) compared to the nominal
 193 1km-by-1km pixel uncertainty $3 \times 10^{-4} \text{ sr}^{-1}$) that this DoF may not be useful for
 194 satellite applications, which we are interested in here. This is corroborated by the DoF < 3
 195 in the next section, despite incorporating the full wavebands of both MODIS-Aqua and
 196 SeaWiFS. Note that when estimating the MODIS-Aqua- and SeaWiFS-equivalent data
 197 from 400–650nm hyperspectral data, the contribution of hyperspectral $R_{rs} > 650\text{nm}$
 198 is not included; while both MODIS-Aqua and SeaWiFS have wavebands centered at $>650\text{nm}$,
 199 these wavebands’ spectral response functions are nonzero for some wavelengths in the
 200 range 400–650nm, and it is only the influence of these hyperspectral wavelengths on all
 201 wavebands that is considered. In other words, $R_{rs}(\lambda)$ is effectively set to zero for all hyper-
 202 spectral wavelengths $>650\text{nm}$ when calculating the multispectral equivalent datasets
 203 in this case.
 204

205 3 Climatologies: R_{rs} versus products

206 The analysis in Section 2 is based on instantaneous, local-scale $R_{rs}(\lambda)$ values measured
 207 in situ at the sea surface. The power of satellite $R_{rs}(\lambda)$ and derived products, how-
 208 ever, lies in their near-continuous global spatial coverage, and many users are primar-
 209 ily interested in climatological data, which is near the coarsest spatial and temporal scales.
 210 In this section we therefore analyze climatological $R_{rs}(\lambda)$ and derived products, again
 211 via PCA to determine DoF.

212 We generated a $1^\circ \times 1^\circ$ climatology for each month using $R_{rs}(\lambda)$ data from Sea-
 213 WiFS spanning 1997–2008, excluding the final 2 years of the mission due to known in-
 214 strument issues (Siegel et al., 2014), using data downloaded from [https://oceancolor](https://oceancolor.gsfc.nasa.gov/)
 215 [.gsfc.nasa.gov/](https://oceancolor.gsfc.nasa.gov/). We did the same for MODIS-Aqua, spanning the time period from
 216 July 2002 – June 2022. We generated analogous climatologies for derived products from
 217 each satellite over the same period and at the same spatial and temporal resolution, namely
 218 the extensive (i.e. mass-dependent) variables Chl, C_{phyto} , POC, PIC, and the intensive
 219 (i.e. mass-independent) variables Z_{eu} , ξ , the fraction of biovolume in the microplank-
 220 ton size class f_{micro} calculated from ξ as described in (Kostadinov et al., 2009), the par-
 221 ticulate backscatter to chlorophyll ratio $b_{bp} : \text{Chl}$, and NPP as estimated by the CAFE
 222 (Silsbe et al., 2016) and CbPMv2 (Westberry et al., 2008) models. Chl, POC, and PIC
 223 were downloaded from <https://oceancolor.gsfc.nasa.gov/>, as was b_{bp} to calculate
 224 C_{phyto} according to (Graff et al., 2015) and $b_{bp} : \text{Chl}$ and the diffuse attenuation coef-
 225 ficient at 490nm to calculate Z_{eu} according to (Lee et al., 2007); SeaWiFS ξ and f_{micro}
 226 were derived as in (Kostadinov et al., 2009); and NPP products were downloaded from
 227 <http://sites.science.oregonstate.edu/ocean.productivity/index.php>. In total
 228 we then have climatologies for MODIS-Aqua, SeaWiFS $R_{rs}(\lambda)$, and ten derived prod-
 229 ucts. We consider the six products Chl, C_{phyto} , POC, PIC, ξ , and Z_{eu} , to be core prod-
 230 ucts and f_{micro} , $b_{bp} : \text{Chl}$, CAFE NPP, and CbPMv2 NPP to be ancillary products as these
 231 are either derived from the core products or rely on ancillary data other than $R_{rs}(\lambda)$.

232 We note that a PCA on the MODIS-Aqua climatologies of $R_{rs}(\lambda)$ and products
 233 other than ξ and f_{micro} yields the same results as those for SeaWiFS below, so we fo-
 234 cus here only on the SeaWiFS climatologies because ξ and f_{micro} are not readily avail-
 235 able for MODIS-Aqua. We find two DoF for SeaWiFS $R_{rs}(\lambda)$, but only one for the prod-
 236 ucts (Figure 4). This result is not sensitive to which combination of products is used –
 237 for instance, including all the ancillary products as well still results in one DoF for the
 238 products. This result is also not sensitive to log-transformations of the variables that are
 239 log-normally (e.g. Chl, POC, PIC, C_{phyto} (Campbell, 1995)) or log-skew-normally (e.g.
 240 NPP, (Cael et al., 2018; Cael, 2021)) distributed, or removal of outliers, zeros, or neg-
 241 ative values.

242 That MODIS-Aqua $R_{rs}(\lambda)$ have three DoF for the data in the previous section but
 243 two DoF from satellite-derived climatologies suggests that some reduction of complex-
 244 ity of the data occurs via some combination of increased sensor noise relative to ship-
 245 based data, atmospheric correction, or averaging over large space and time scales (Scott
 246 & Werdell, 2019). (Note (Scott & Werdell, 2019) also point out the difference between
 247 averaging $R_{rs}(\lambda)$ versus taking the ratio of averaged water-leaving radiance Lw and down-
 248 welling irradiance, which may introduce a slight bias but is unlikely to affect our results
 249 here.) Two DoF remain in satellite climatological $R_{rs}(\lambda)$ for both SeaWiFS and MODIS-
 250 Aqua, indicating the possibility of generating two independent products from these data.
 251 The suite of products tested above, however, has one fewer DoF than the $R_{rs}(\lambda)$. This
 252 is likely due to derived products’ appreciable uncertainties and/or strong correlations
 253 with chlorophyll. POC, ξ , and Z_{eu} , for instance, have Spearman rank correlations (across
 254 all months and 1° grid cells) of >0.9 with Chl. C_{phyto} ’s rank correlation with Chl is still
 255 fairly high, at 0.61, and is low largely due to small fluctuations when both are small; a
 256 simple spline fit of $\log(C_{phyto})$ against $\log(\text{Chl})$ yields an r^2 of 0.7.

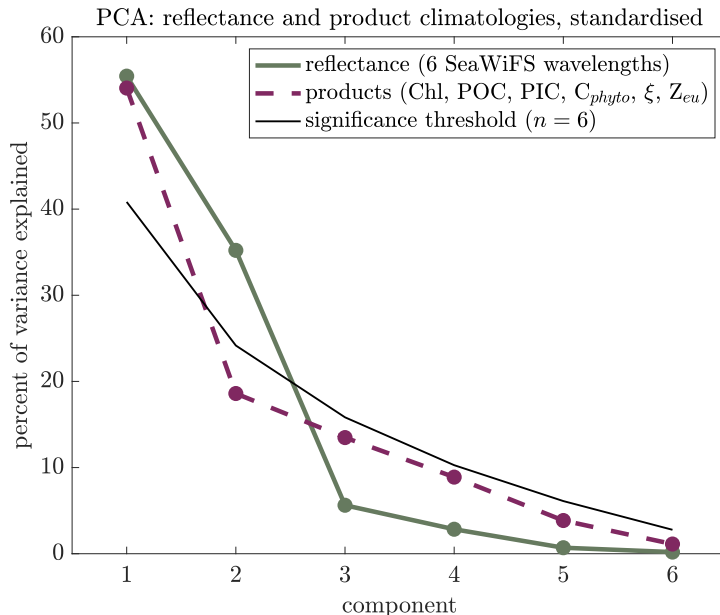


Figure 4. Scree plot of percent variance explained versus component for climatologies of SeaWiFS $R_{rs}(\lambda)$ and of six SeaWiFS- $R_{rs}(\lambda)$ -derived products. Black line indicates broken-stick significance threshold for six-dimensional data.

257 The exception is PIC, which has a rank correlation with Chl of 0.11. PIC, how-
 258 ever, is highly sensitive to small variations in $R_{rs}(\lambda)$ for typical $R_{rs}(\lambda)$ values. To sub-
 259 stantiate this, we performed a simple sensitivity analysis with the standard two-band PIC
 260 algorithm used by NASA for all but the most optically bright waters (see [https://oceancolor](https://oceancolor.gsfc.nasa.gov/atbd/pic/)
 261 [.gsfc.nasa.gov/atbd/pic/](https://oceancolor.gsfc.nasa.gov/atbd/pic/)). We calculated PIC for the climatological median $R_{rs}(\lambda)$
 262 at 443 nm and 555 nm and for 5% variations, converting to normalized water-leaving ra-
 263 diance by multiplying by the global mean extraterrestrial solar irradiance. We then per-
 264 turbed these $R_{rs}(\lambda)$ values with Gaussian noise at the 5% level, corresponding to the
 265 nominal uncertainty in $R_{rs}(\lambda)$. This noise at 443 nm results in 68% noise in PIC. By con-
 266 trast, POC only varies 5% with these 5% variations in $R_{rs}(\lambda)$ at either wavelength. This
 267 indicates that in the bulk of cases, satellite-derived PIC is highly uncertain, on the or-
 268 der of 70% (and note the PIC uncertainty will be magnified more when considering docu-
 269 mented uncertainties for $R_{rs}(\lambda)$ of 15-40% in some regions (Bisson et al., 2021)). In con-
 270 trast, for relatively bright waters, the same exercise resulted in PIC variations of <10%,
 271 indicating that this algorithm performs well in instances when PIC values are high. Nonethe-
 272 less, the high sensitivity to typical uncertainty in $R_{rs}(\lambda)$ for median waters explains why
 273 we find one DoF for the products even though PIC and Chl are not strongly correlated:
 274 derived PIC is noisy most of the time.

275 These results have two key implications. One is that there is additional informa-
 276 tion in climatological $R_{rs}(\lambda)$ that is not included in current derived products. This im-
 277 plies that existing products do not utilize the full set of $R_{rs}(\lambda)$ wavelengths. The other
 278 implication is that these products are not at all independent, and should not be treated
 279 as such when using them simultaneously. In other words, there are more products than
 280 there are DoF in satellite data. A numerical ecosystem model that reproduces the satellite-
 281 derived climatology of chlorophyll and of the particle size distribution’s spectral slope
 282 should not be considered to be capturing two independent properties of the Earth sys-

283 tem. When using satellite products as inputs to other models, these products and their
 284 propagated uncertainties must be treated simultaneously rather than independently.

285 The results presented here are appropriate for global ocean analyses. The open ocean
 286 represents the largest area, and is composed primarily of Case 1 waters; that is, waters
 287 in which optical variability is dominated by chlorophyll (Morel & Prieur, 1977). In this
 288 context, it is in a sense unsurprising that the suite of $R_{rs}(\lambda)$ -derived products produced
 289 only one DoF. More optically complex waters, such as coastal regions and inland waters,
 290 have optical variability that is influenced by other constituents, such as colored dissolved
 291 organic material (CDOM), inorganic particles, and other pigments in addition to chloro-
 292 phyll (e.g. Brown et al., 2008; Nelson & Siegel, 2013)). Analyses focused on these wa-
 293 ters is likely to reveal a higher number of DoF from both $R_{rs}(\lambda)$ and derived products.
 294 Indeed, algorithms to derive concentrations of cyanobacteria and suspended particulate
 295 (Wang et al., 2016)) or distinguish between different phytoplankton species (Erickson
 296 et al., 2020) can be successful in such waters. However, we note that the in situ dataset
 297 used here (Figure 1) represents waters with $R_{rs}(\lambda)$ variability similar to that of the ocean
 298 as a whole, which can be seen by comparing the variation in $R_{rs}(\lambda)$ at each MODIS-Aqua
 299 wavelength from global satellite data with the same satellite data sub-sampled to the lo-
 300 cations with in situ measurements (or the closest non-cloudy location). Sub-sampled satel-
 301 lite measurements have similar, and slightly lower, $R_{rs}(\lambda)$ in bluer wavelengths, indicat-
 302 ing that the in situ dataset is oriented more towards optically complex coastal waters
 303 with substantial CDOM. This suggests that part of the explanation for the drop in DoF
 304 in satellite-derived climatologies comes from the fact that the in situ dataset sampled,
 305 as a whole, more optically complex waters.

306 We find that both $R_{rs}(\lambda)$ and variables derived from $R_{rs}(\lambda)$ are highly inter-correlated,
 307 reducing the number of DoF associated with each, with a greater reduction in DoF in
 308 the derived products. This becomes a problem when products are derived using empir-
 309 ical relationships with $R_{rs}(\lambda)$, and especially when the same wavelengths are used for
 310 the products that are assumed to be independent of each other; for example, over much
 311 of the ocean PIC, POC, and chlorophyll all are functions only of $R_{rs}(\lambda)$ at two wave-
 312 lengths, at (or near, depending on the sensor) 443 and 555 nm. Certain combinations
 313 of PIC, POC, and chlorophyll, which may occur in the surface ocean, are therefore im-
 314 possible to find using these algorithms. This is distinct from algorithms, typically called
 315 “quasi-analytical” or “semi-empirical”, that use known or assumed spectral shapes for
 316 absorption and scattering properties of optical constituents that can be related to the
 317 same derived products, such as PIC, POC, and chlorophyll (Werdell et al., 2013). These
 318 approaches may result in similar correlations and DoF between derived products, but
 319 do not inherently have the same problems as empirical approaches. We note that PACE
 320 will have, in addition to hyperspectral visible bands, UV bands from 350nm as well as
 321 spectral polarized bands. These measurements are expected to both improve the atmo-
 322 spheric correction (hence reduce the $R_{rs}(\lambda)$ uncertainties) as well as provide their own
 323 ocean signals, both of which may increase the DoF compared to those found here. In ad-
 324 dition, it has been shown that adding other environmental variables such as SST can add
 325 useful information to inversions of phytoplankton groups (e.g. Chase et al., 2022) and
 326 thus another approach to increase DoF for inversions by adding relevant and indepen-
 327 dent information (e.g. mixed-layer depth and nutrients from BGC-Argo assimilating mod-
 328 els).

329 4 Conclusion

330 The results presented here highlight the high degree of co-dependence between re-
 331 mote sensing reflectances at different wavelengths and of the products derived from these
 332 reflectances. For users of products based on existing reflectances, this primarily means
 333 factoring in the relationships between products when using more than one simultane-
 334 ously. For the algorithms that generate these products from existing reflectances, these

335 results indicate a potential to improve the suite of available products to be more accu-
 336 rate and precise, and to account for the relationships between products and $R_{rs}(\lambda)$ wave-
 337 bands. One way to do this, consistent with the findings above, would be to derive a sin-
 338 gular product such as chlorophyll as a function of all reflectance wavebands, derive an anomaly
 339 from chlorophyll-based expectations of a secondary product (e.g., phytoplankton com-
 340 munity composition, size, POC, PIC, and so forth), then specify all other products ex-
 341 plicitly as a function of these two, along the lines of Alvain et al. (2005). Ancillary and
 342 independent information can also be added to algorithms, as is currently done with net
 343 primary production models via temperature and mixed layer depth.

344 These findings are most relevant for algorithms that will generate products from
 345 hyperspectral reflectances in the future. The small number of degrees of freedom in hy-
 346 perspectral reflectances indicates that only a few quantities can be estimated independ-
 347 ently, and that different wavelengths' reflectances as measured from space will be strongly
 348 correlated. Complex algorithms that utilize the full spectrum of reflectance will need to
 349 factor in these correlations in order to generate reliable products. Crucially, if more than
 350 a few products are generated from hyperspectral reflectances, as is likely the case, such
 351 algorithms will also need to output the covariance information encoding the uncertainty
 352 in each product and the relationships between them. This can be achieved by some, but
 353 not all, machine learning techniques, on which this new generation of algorithms are likely
 354 to be based. The fact that hyperspectral reflectances can be predicted within nominal
 355 uncertainties by their multispectral equivalents suggests that hyperspectral resolution
 356 can play a role in improving ocean color products, but that it will be challenging to pro-
 357 vide a substantially finer-grained picture of surface ocean ecosystems and biogeochem-
 358 ical cycles. Here by relying on principal component analysis we have focused on broad,
 359 first-order variations, but where such resolution may be most useful and generate novel
 360 insights is in investigating outliers and rare events, such as blooms or binning data over
 361 coherent features like eddies, where e.g. monospecific signatures may be resolved with
 362 spectral precision.

363 Open Research

364 Remote sensing data were downloaded from <https://oceancolor.gsfc.nasa.gov/>
 365 and <http://sites.science.oregonstate.edu/ocean.productivity/index.php>. All
 366 data and code are available at github.com/bbcael/eifoc for review purposes and will
 367 be given a Zenodo DOI should this manuscript be accepted for publication.

368 Acknowledgments

369 It is a pleasure to thank the many scientists whose collective work has generated the data
 370 on which this work relies. Cael acknowledges support from the National Environmen-
 371 tal Research Council through Enhancing Climate Observations, Models and Data, and
 372 the European Union's Horizon 2020 Research and Innovation Programme under grant
 373 agreement No. 820989 (project COMFORT). The work reflects only the authors' view;
 374 the European Commission and their executive agency are not responsible for any use that
 375 may be made of the information the work contains. KB acknowledges support from NASA
 376 grant 80NSSC18K0957. EB acknowledges support from NASA grant 80NSSC20M0203.
 377 Cael lead and all other authors assisted with all aspects of this work. The authors have
 378 no competing interests to declare. This is PMEL contribution number 5445.

379 References

380 Alvain, S., Moulin, C., Dandonneau, Y., & Breon, F.-M. (2005). Remote sensing of
 381 phytoplankton groups in case 1 waters from global seawifs imagery. *Deep Sea*
 382 *Research Part I: Oceanographic Research Papers*, 52(11), 1989–2004.

- 383 Behrenfeld, M. J., & Falkowski, P. G. (1997). Photosynthetic rates derived from
 384 satellite-based chlorophyll concentration. *Limnology and oceanography*, *42*(1),
 385 1–20.
- 386 Bisson, K., Boss, E., Werdell, P. J., Ibrahim, A., Frouin, R., & Behrenfeld, M.
 387 (2021). Seasonal bias in global ocean color observations. *Applied optics*,
 388 *60*(23), 6978–6988.
- 389 Bisson, K., Siegel, D. A., & DeVries, T. (2020). Diagnosing mechanisms of ocean
 390 carbon export in a satellite-based food web model. *Frontiers in Marine Sci-*
 391 *ence*, *7*, 505.
- 392 Brown, C. A., Huot, Y., Werdell, P. J., Gentili, B., & Claustre, H. (2008). The
 393 origin and global distribution of second order variability in satellite ocean
 394 color and its potential applications to algorithm development. *Remote*
 395 *Sensing of Environment*, *112*(12), 4186–4203. Retrieved from [https://](https://www.sciencedirect.com/science/article/pii/S0034425708002162)
 396 www.sciencedirect.com/science/article/pii/S0034425708002162 doi:
 397 <https://doi.org/10.1016/j.rse.2008.06.008>
- 398 Cael, B. (2021). Variability-based constraint on ocean primary production models.
 399 *Limnology and Oceanography Letters*, *6*(5), 262–269.
- 400 Cael, B., Bisson, K., & Follett, C. L. (2018). Can rates of ocean primary production
 401 and biological carbon export be related through their probability distributions?
 402 *Global biogeochemical cycles*, *32*(6), 954–970.
- 403 Cael, B., Bisson, K., & Follows, M. J. (2017). How have recent temperature changes
 404 affected the efficiency of ocean biological carbon export? *Limnology and*
 405 *Oceanography Letters*, *2*(4), 113–118.
- 406 Cael, B., Chase, A., & Boss, E. (2020). Information content of absorption spectra
 407 and implications for ocean color inversion. *Applied Optics*, *59*(13), 3971–3984.
- 408 Cael, B., Dutkiewicz, S., & Henson, S. (2021). Abrupt shifts in 21st-century plank-
 409 ton communities. *Science advances*, *7*(44), eabf8593.
- 410 Campbell, J. W. (1995). The lognormal distribution as a model for bio-optical vari-
 411 ability in the sea. *Journal of Geophysical Research: Oceans*, *100*(C7), 13237–
 412 13254.
- 413 Chase, A. P., Boss, E., Cetinić, I., & Slade, W. (2017). Estimation of phytoplankton
 414 accessory pigments from hyperspectral reflectance spectra: toward a global
 415 algorithm. *Journal of Geophysical Research: Oceans*, *122*(12), 9725–9743.
- 416 Chase, A. P., Boss, E. S., Haëntjens, N., Culhane, E., Roesler, C., & Karp-Boss,
 417 L. (2022). Plankton imagery data inform satellite-based estimates of diatom
 418 carbon. *Geophysical Research Letters*, *49*(13), e2022GL098076. Retrieved
 419 from [https://agupubs.onlinelibrary.wiley.com/doi/abs/10.1029/](https://agupubs.onlinelibrary.wiley.com/doi/abs/10.1029/2022GL098076)
 420 [2022GL098076](https://agupubs.onlinelibrary.wiley.com/doi/abs/10.1029/2022GL098076) (e2022GL098076 2022GL098076) doi: [https://doi.org/10.1029/](https://doi.org/10.1029/2022GL098076)
 421 [2022GL098076](https://doi.org/10.1029/2022GL098076)
- 422 DeVries, T., & Weber, T. (2017). The export and fate of organic matter in the
 423 ocean: New constraints from combining satellite and oceanographic tracer
 424 observations. *Global Biogeochemical Cycles*, *31*(3), 535–555.
- 425 Dutkiewicz, S., Cermenó, P., Jahn, O., Follows, M. J., Hickman, A. E., Taniguchi,
 426 D. A., & Ward, B. A. (2020). Dimensions of marine phytoplankton diversity.
 427 *Biogeosciences*, *17*(3), 609–634.
- 428 Erickson, Z. K., Werdell, P. J., & Cetinić, I. (2020). Bayesian retrieval of optically
 429 relevant properties from hyperspectral water-leaving reflectances. *Applied Op-*
 430 *tics*, *59*(23), 6902–6917. doi: 10.1364/AO.398043
- 431 Evers-King, H., Martínez-Vicente, V., Brewin, R. J., Dall’Olmo, G., Hickman, A. E.,
 432 Jackson, T., ... others (2017). Validation and intercomparison of ocean color
 433 algorithms for estimating particulate organic carbon in the oceans. *Frontiers*
 434 *in Marine Science*, 251.
- 435 Gordon, H. R., & Wang, M. (1994). Retrieval of water-leaving radiance and aerosol
 436 optical thickness over the oceans with seawifs: a preliminary algorithm. *Ap-*
 437 *plied optics*, *33*(3), 443–452.

- 438 Graff, J. R., Westberry, T. K., Milligan, A. J., Brown, M. B., Dall’Olmo, G., van
439 Dongen-Vogels, V., . . . Behrenfeld, M. J. (2015). Analytical phytoplankton
440 carbon measurements spanning diverse ecosystems. *Deep Sea Research Part I:
441 Oceanographic Research Papers*, 102, 16–25.
- 442 Hovis, W. A., Clark, D., Anderson, F., Austin, R., Wilson, W., Baker, E., . . . others
443 (1980). Nimbus-7 coastal zone color scanner: system description and initial
444 imagery. *Science*, 210(4465), 60–63.
- 445 Hu, C., Lee, Z., & Franz, B. (2012). Chlorophyll algorithms for oligotrophic oceans:
446 A novel approach based on three-band reflectance difference. *Journal of Geo-
447 physical Research: Oceans*, 117(C1).
- 448 Huot, Y., & Antoine, D. (2016). Remote sensing reflectance anomalies in the ocean.
449 *Remote Sensing of Environment*, 184, 101–111. doi: 10.1016/j.rse.2016.06.002
- 450 Jackson, D. A. (1993). Stopping rules in principal components analysis: a compari-
451 son of heuristical and statistical approaches. *Ecology*, 74(8), 2204–2214.
- 452 Kostadinov, T., Siegel, D., & Maritorena, S. (2009). Retrieval of the particle size
453 distribution from satellite ocean color observations. *Journal of Geophysical Re-
454 search: Oceans*, 114(C9).
- 455 Kramer, S. J., Siegel, D. A., Maritorena, S., & Catlett, D. (2022). Modeling surface
456 ocean phytoplankton pigments from hyperspectral remote sensing reflectance
457 on global scales. *Remote Sensing of Environment*, 270, 112879.
- 458 Lee, Z., Weidemann, A., Kindle, J., Arnone, R., Carder, K. L., & Davis, C. (2007).
459 Euphotic zone depth: Its derivation and implication to ocean-color remote
460 sensing. *Journal of Geophysical Research: Oceans*, 112(C3).
- 461 Mitchell, C., Hu, C., Bowler, B., Drapeau, D., & Balch, W. (2017). Estimating par-
462 ticulate inorganic carbon concentrations of the global ocean from ocean color
463 measurements using a reflectance difference approach. *Journal of Geophysical
464 Research: Oceans*, 122(11), 8707–8720.
- 465 Morel, A., & Prieur, L. (1977). Analysis of variations in ocean color 1. *Limnology
466 and oceanography*, 22(4), 709–722.
- 467 Nelson, N. B., & Siegel, D. A. (2013). The global distribution and dynamics of chro-
468 mophoric dissolved organic matter. *Annual review of marine science*, 5, 447–
469 476.
- 470 Nowicki, M., DeVries, T., & Siegel, D. A. (2022). Quantifying the carbon export and
471 sequestration pathways of the ocean’s biological carbon pump. *Global Biogeo-
472 chemical Cycles*, 36(3), e2021GB007083.
- 473 O’Reilly, J. E., Maritorena, S., Mitchell, B. G., Siegel, D. A., Carder, K. L., Garver,
474 S. A., . . . McClain, C. (1998). Ocean color chlorophyll algorithms for seawifs.
475 *Journal of Geophysical Research: Oceans*, 103(C11), 24937–24953.
- 476 Scholz, M., Fraunholz, M., & Selbig, J. (2008). Nonlinear principal component anal-
477 ysis: neural network models and applications. In *Principal manifolds for data
478 visualization and dimension reduction* (pp. 44–67). Springer.
- 479 Scott, J. P., & Werdell, P. J. (2019). Comparing level-2 and level-3 satellite ocean
480 color retrieval validation methodologies. *Optics Express*, 27(21), 30140–30157.
- 481 Siegel, D., Buesseler, K., Doney, S. C., Sailley, S., Behrenfeld, M. J., & Boyd, P.
482 (2014). Global assessment of ocean carbon export by combining satellite obser-
483 vations and food-web models. *Global Biogeochemical Cycles*, 28(3), 181–196.
- 484 Silsbe, G. M., Behrenfeld, M. J., Halsey, K. H., Milligan, A. J., & Westberry, T. K.
485 (2016). The cafe model: A net production model for global ocean phytoplank-
486 ton. *Global Biogeochemical Cycles*, 30(12), 1756–1777.
- 487 Wang, G., Lee, Z., Mishra, D. R., & Ma, R. (2016). Retrieving absorption coef-
488 ficients of multiple phytoplankton pigments from hyperspectral remote sens-
489 ing reflectance measured over cyanobacteria bloom waters. *Limnology and
490 Oceanography: Methods*, 14(7), 432–447. doi: 10.1002/lom3.10102
- 491 Weinberger, K. Q., Sha, F., & Saul, L. K. (2004). Learning a kernel matrix for non-
492 linear dimensionality reduction. In *Proceedings of the twenty-first international*

- 493 *conference on machine learning* (p. 106).
- 494 Werdell, P. J., Behrenfeld, M. J., Bontempi, P. S., Boss, E., Cairns, B., Davis,
495 G. T., ... others (2019). The plankton, aerosol, cloud, ocean ecosystem
496 mission: status, science, advances. *Bulletin of the American Meteorological*
497 *Society*, 100(9), 1775–1794.
- 498 Werdell, P. J., Franz, B. A., Bailey, S. W., Feldman, G. C., Boss, E., Brando, V. E.,
499 ... others (2013). Generalized ocean color inversion model for retrieving
500 marine inherent optical properties. *Applied Optics*, 52(10), 2019–2037.
- 501 Westberry, T., Behrenfeld, M., Siegel, D., & Boss, E. (2008). Carbon-based primary
502 productivity modeling with vertically resolved photoacclimation. *Global Bio-*
503 *geochemical Cycles*, 22(2).
- 504 Wold, S., Esbensen, K., & Geladi, P. (1987). Principal component analysis. *Chemo-*
505 *metrics and intelligent laboratory systems*, 2(1-3), 37–52.